nature communications

Article

https://doi.org/10.1038/s41467-024-54701-4

Quantum quench dynamics of geometrically frustrated Ising models

Received: 27 April 2024

Accepted: 15 November 2024

Published online: 30 December 2024

Check for updates

Ammar Ali[1,6], Hanjing Xu[2,6], William Bernoudy[3], Alberto Nocera[4,5], Andrew D. King[3] ✉ & Arnab Banerjee[1] ✉

Geometric frustration in two-dimensional Ising models allows for a wealth of exotic universal behavior, both Ising and non-Ising, in the presence of quantum fluctuations. In particular, the triangular antiferromagnet and Villain model in a transverse field can be understood through distinct XY pseudospins, but have qualitatively similar phase diagrams including a quantum phase transition in the (2+1)-dimensional XY universality class. While the quantum dynamics of modestly-sized systems can be simulated classically using tensor-based methods, these methods become infeasible for larger lattices. Here we perform both classical and quantum simulations of these dynamics, where our quantum simulator is a superconducting quantum annealer. Our observations on the triangular lattice suggest that the dominant quench dynamics are not described by the quantum Kibble-Zurek scaling of the quantum phase transition, but rather a faster coarsening dynamics in an effective two-dimensional XY model in the ordered phase. Similarly, on the Villain model, the scaling exponent does not match the Kibble-Zurek expectation. These results demonstrate the ability of quantum annealers to perform coherent quantum dynamics simulations that are hard to classically scale beyond small systems, and open the avenue to predictive simulations of the dynamics of Ising magnetic materials on quantum simulators.

Frustrated systems are systems in which it is impossible to simultaneously minimize all Hamiltonian terms, either due to the non-commutativity of the terms or the lattice geometry (geometric frustration). Such models are of great interest in both classical and quantum spin systems due to their ability to maintain topological order, by giving rise to topologically protected quasi-particle excitations, and host topological defects, such as 1D kinks, 2D vortices, domain walls, etc.[1–6].

Focusing on geometric frustration and its defects, two closely related models of particular relevance to quantum systems are classical stacked frustrated magnets: the 3D antiferromagnetic (AFM) triangular Ising model[7], and the 3D frustrated Ising simple cubic lattice[8], both of which are known to undergo thermal phase transition that belongs to the 3D XY universality class[7,8]. By virtue of the classical-quantum duality[9], the 2D quantum versions of these systems are expected to have quantum phase transitions belonging to the same universality class[10]. Indeed, the 2D Transverse Field Ising Model (TFIM) on an AFM triangular lattice turned out to have a quantum critical point in the 3D XY universality class (Fig. 1a)[3,11,12]. Similarly, the TFIM on a fully frustrated square lattice, known as the Villain model[13], was shown to share the same critical behavior[3].

Simulation of a frustrated system on a quantum annealer (QA) was realized in[14] where the thermal Kosterlitz–Thouless (KT) phase transition[15] was observed. Correlations between the topological

[1]Department of Physics and Astronomy, Purdue University, West Lafayette, IN, USA. [2]Department of Computer Science, Purdue University, West Lafayette, IN, USA. [3]D-Wave Quantum Inc., Burnaby, BC, Canada. [4]Stewart Blusson Quantum Matter Institute, University of British Columbia, Vancouver, BC, Canada. [5]Department of Physics Astronomy, University of British Columbia, Vancouver, BC, Canada. [6]These authors contributed equally: Ammar Ali, Hanjing Xu. ✉e-mail: aking@dwavesys.com; arnabb@purdue.edu

https://doi.org/10.1038/s41467-024-54701-4

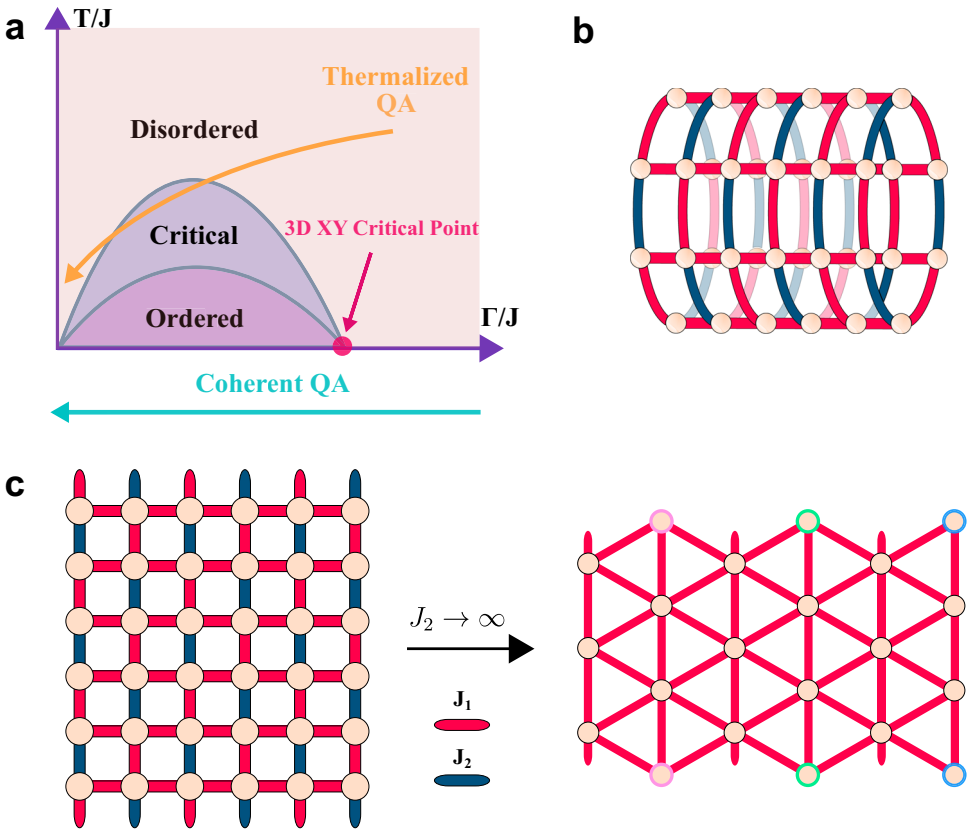

Fig. 1 | Phase diagram and lattice definition. a Qualitative phase diagram of the triangular and Villain TFIMs (adapted from[3]). The orange arrow shows the KT phase transition explored in[14], while the cyan arrow depicts the path considered in this work, passing through the 3D XY quantum critical point. **b** Embedded lattice on the quantum annealer (QA) corresponds to a square lattice with periodic boundary conditions along one direction giving a cylinder. **c** Shown is the choice of couplings and the contraction to an AFM triangular lattice when taking the magnitude of the FM couplers (J_2) to be much larger than the AFM ones (J_1). Nodes sharing the same border color are identified.

defects—vortices and antivortices—were shown to have an exponential decay above the critical temperature and a power-law decay below it, showcasing the binding of defects into vortex-antivortex pairs and establishing their quasi-long-range order. In ref. 16, it was shown that simulating finite-temperature frustrated quantum systems on QAs greatly accelerates the computational performance where a speedup up to 10^6 was reported over Path-Integral Monte Carlo simulation (PIMC), a leading classical method[16]. In the same vein, it was lately shown in[17] that approximate optimization on QAs has a scaling advantage over the classical heuristic algorithm parallel tempering with isoenergetic cluster moves (PT-ICM). The frustrated Kagome lattice was also studied where its equilibrium phase diagram was simulated[18]. More recently, coherent quantum annealing has been demonstrated in superconducting processors, allowing quantum simulation of programmable geometries on thousands of qubits with negligible coupling to the thermal environment.

Coherent quantum annealing was first realized in ref. 19 where they studied the quenching of a 1D TFIM chain. It was shown that the defect density ρ resulting from the equilibration of the chain into alternating $\mathbb{Z}_2$ ordered domains follows the Kibble–Zurek mechanism (KZM) scaling[20,21]

$$\rho \propto t_a^{\frac{-d\nu}{1+z\nu}}, \tag{1}$$

where t_a is the annealing time, d is the space dimensionality, z and ν are the dynamical and correlation length critical exponents of the 2D Ising universality class, respectively. For later use, we also introduce the critical exponent β, which quantifies the vanishing of the order parameter upon approaching the critical point from the ordered phase. KZM was also observed on a 1D Rydberg atom array in ref. 22, where also $\mathbb{Z}_3$ and $\mathbb{Z}_4$ broken-order phases were explored, and on a 2D Rydberg atom square array in ref. 23. Further coherent quantum dynamics were observed in a 3D spin glass system where a scaling advantage of quantum annealing over both simulated annealing and simulated quantum annealing was reported[24]. More recently, this was expanded to 2D and infinite-dimensional spin glasses, and intractability of classical simulation approaches was explored[25].

In this work, we explore the quenching of 2D frustrated systems, namely the AFM TFIM triangular and Villain models. Figure 1b and c shows the considered lattice, a square lattice of size $L \times L$ with periodic boundary conditions along the vertical direction. Our results indicate that a coarsening mechanism governs the scaling laws of the systems when quenched to a final state deep into the ordered phase, as opposed to the expected KZM. During the course of the review process, the authors became aware of two related works that study the coarsening dynamics of similar models on an analog[26] and an analog-digital[27] quantum devices.

Results and discussion

The D-Wave Advantage QA realizes the TFIM Hamiltonian

$$\mathcal{H}(s) = -\Gamma(s)\sum_i \sigma_i^x + \mathcal{J}(s)\sum_{\langle ij\rangle} J_{ij}\sigma_i^z\sigma_j^z, \tag{2}$$

where s is the normalized time t/t_a going from 0 to 1. The parameters $\Gamma(s)$ and $\mathcal{J}(s)$ evolve monotonically such that $\Gamma(0) = \mathcal{J}(1) = 1$ and $\Gamma(1) = \mathcal{J}(0) = 0$. We denote by the triangular lattice the choice of couplers $J_1 = +0.9, J_2 = -2$, and by the Villain model the choice $J_1 = -J_2 = 0.9$,

https://doi.org/10.1038/s41467-024-54701-4

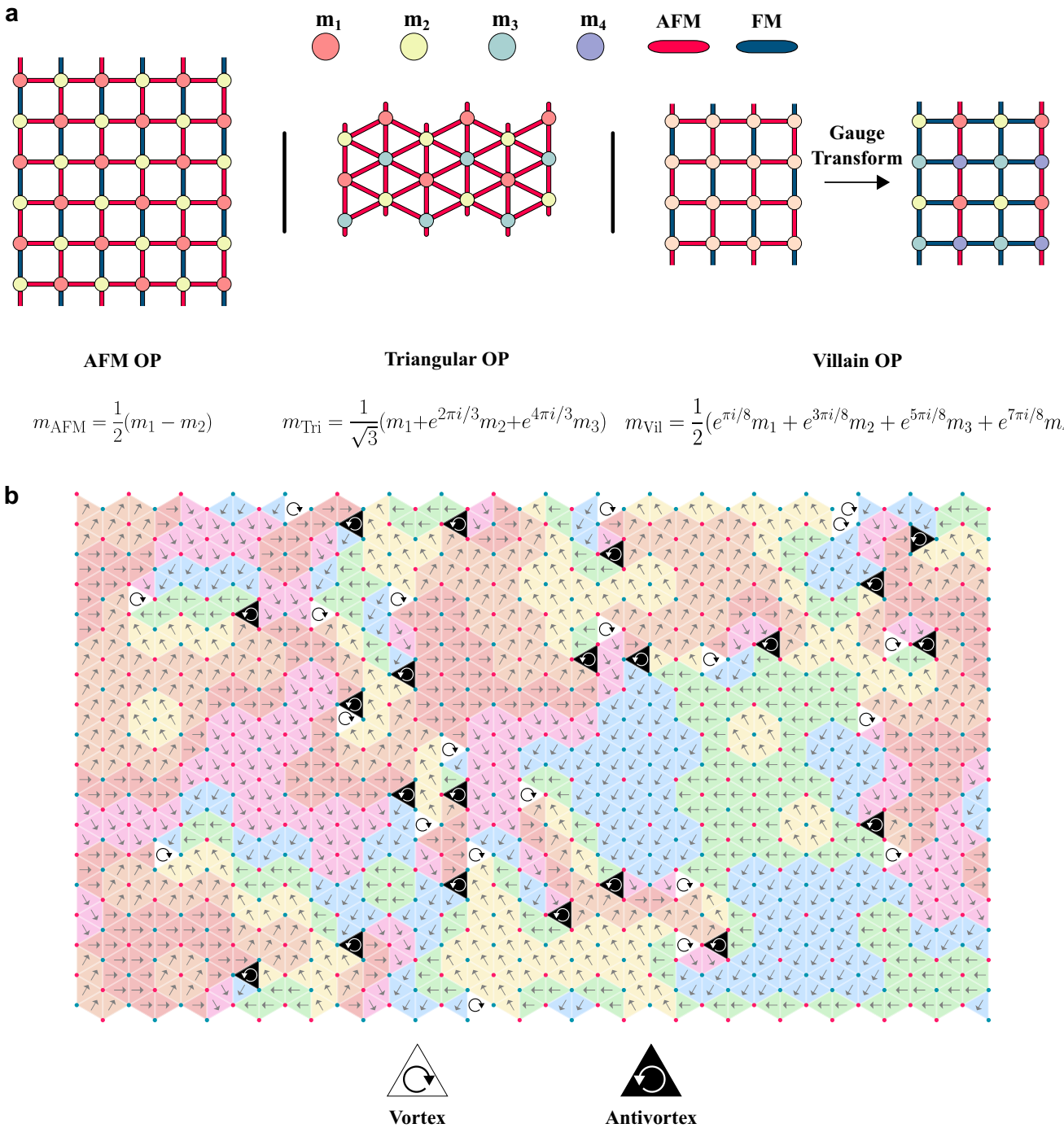

Fig. 2 | Order parameters (OPs) definitions and topological defects. a Pictorial representation of the three different OPs, given in Eqs. (4)–(6). **b** A triangular lattice QA output instance for $L = 36$, and $t_a = 6.3$ ns. The pseudospin of each plaquette is indicated giving rise to the topological defects (polarized plaquettes, i.e. all spins pointing along the same direction) represented by the vortices (white) and antivortices (black).

where we will be presenting, to our knowledge, its first experimental realization. Figure 1c shows how such a choice approximates the square lattice as a triangular one by contracting every other pair of physical qubits into one logical qubit.

Initially, all qubits are prepared in the superposition state

$$|\rightarrow\rangle = \frac{1}{\sqrt{2}}|\uparrow\rangle + \frac{1}{\sqrt{2}}|\downarrow\rangle, \tag{3}$$

which is the ground state of the initial Hamiltonian $\mathcal{H}(0)$. Evolving slowly enough from this ground state, the adiabatic theorem guarantees that we always stay at the instantaneous ground state. However, by quenching the system we generally end up in an excited state, whose scaling with quenching time depends on the underlying mechanism governing the dynamics, e.g. KZM or coarsening dynamics. We aim to characterize the scaling of these frustrated systems by quantifying the scaling of the order parameters (OPs) (Fig. 2a), defect density (Fig. 2b), and correlation lengths.

https://doi.org/10.1038/s41467-024-54701-4

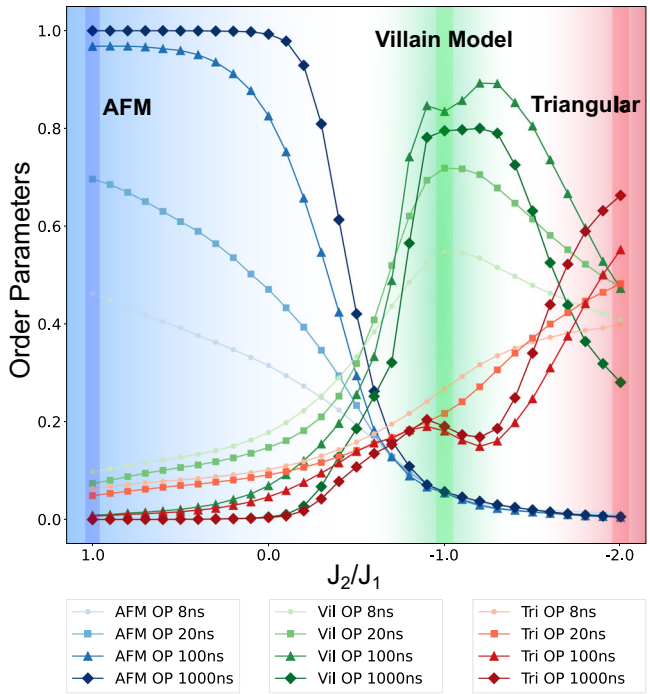

Fig. 3 | OPs as a function of the ratio J_2/J_1. Evolution of the different OPs evaluated on a 12 × 12 lattice while fixing J_1 to be + 0.9 and varying J_2 to span the ratio range from +1 (AFM square lattice) to − 2 (triangular lattice approximation). We observe different regimes in which each OP is maximum. We also observe how the OPs change with changing total annealing time where we note that generally, increasing annealing time leads to increased order, i.e. approaching the classical ground state. But interestingly, this is not the case for the Villain OP indicating the influence of quantum fluctuations on its ordering. Source data are provided as a Source Data file.

The three OPs m_{AFM}, m_{Tri}, and m_{Vil} are defined by dividing the lattice into two, three, and four sublattices, respectively, as depicted in Fig. 2a. They are given by ([11,28])

$$m_{\mathrm{AFM}} = \frac{1}{2}(m_1 - m_2), \tag{4}$$

$$m_{\mathrm{Tri}} = \frac{1}{\sqrt{3}}(m_1 + e^{2\pi i/3} m_2 + e^{4\pi i/3} m_3), \tag{5}$$

$$m_{\mathrm{Vil}} = \frac{1}{2}(e^{\pi i/8} m_1 + e^{3\pi i/8} m_2 + e^{5\pi i/8} m_3 + e^{7\pi i/8} m_4), \tag{6}$$

where m_i, $i \in 1, 2, 3, 4$, is the magnetization of the ith sublattice. We note that due to their sublattice structure, triangular (Villain) OPs are only defined for lattice dimensions multiple of three (four).

Figure 3 probes the evolution of the three OPs on a 12 × 12 lattice in which we fix the J_1 couplers to + 0.9 and allow J_2 to go from $J_2 = J_1$, i.e. square AFM lattice, to $J_2 = -2J_1$, which is the triangular approximation as shown in Fig. 1c. We perform this for increasing values of annealing times 8 ns, 20 ns, 100 ns, and 1 μs, and measure the OPs of the final evolved state. We identify different regions in the parameter space in which each OP is maximum, highlighting the phase of the system. Due to the hardware constraints, we were not able to extend the parameters to the region in which the triangular OP m_{Tri} is maximized, as it is still seen to increase at the limiting ratio $J_2/J_1 = -2$.

As annealing time is increased, the magnitudes of the AFM and triangular OPs are observed to increase, which indicates that the systems are approaching their respective ground states (classical ground state for m_{AFM} and perturbative one for m_{Tri}). However, we notice that this is not the case for Villain OP m_{Vil} as it appears to be maximally ordered for an intermediate annealing time which means that this phase is quantum-ordered. In other words, this phase is more sensitive to noise and its thermal state is less ordered than its quantum-quenched state, warranting further study such as the recent[28]. Now, we would like to quantify the scaling of the OPs with annealing time.

In Fig. 4a, c, we compute the scaling of m_{Tri}, and m_{Vil} w.r.t. annealing time for different lattice sizes where we find consistent power-law behavior. The OPs are still seen to increase towards the end of the interval indicating that the systems are yet to reach their respective ground states (for a longer interval plot see Supplementary Fig. 8, where we explain the deviation from the scaling behavior at long annealing times beyond coherence time). Crucially, in Fig. 4a, we compare the QA results with matrix product states (MPSs) simulation using the time-dependent variational principle (TDVP) algorithm for time evolution on the 6 × 6 lattice size. We observe quantitative agreement in this comparison, verifying coherent quantum dynamics (For more details about the MPS-TDVP simulations and convergence analysis, see Methods Section 10). We also observe in Fig. 4b and d the collapse of the OPs for the different sizes when scaled by the linear system size L. While the collapse appears to be better for the larger system sizes due to the saturation of small systems' OPs, it indicates universal physics independent of the system size for the collapsed instances. Nonetheless, although the MPS simulations are known to be computationally expensive and non-scalable in two dimensions (exponential scaling in the size of the cylinder circumference length[29,30]), scaling on the QA comes with no noticeable overhead, proving the advantage of using QAs as coherent quantum simulators.

We report the scaling exponents for the OPs on the largest size $L = 36$ (1296 qubits equivalent to 648 logical qubits in the triangular lattice):

$$m_{\mathrm{Tri}} \propto t_a^{0.35(4)}, m_{\mathrm{Vil}} \propto t_a^{0.46(2)}. \tag{7}$$

The triangular and Villain models belong to the 3D XY universality class[3] for which $\nu = 0.67175(10)$, $\beta = 0.34869(7)$[31,32], and $z = 1$ for an isotropic Lorentz-invariant theory[33]; therefore KZM predicts the critical scaling exponent

$$m \propto t_a^{\frac{1-\beta/\nu}{z+1/\nu}} = t_a^{0.19}, \tag{8}$$

which does not agree with the observed exponents. To explain this discrepancy, we perform a Monte Carlo (MC) simulation (details in Methods) on the six-state clock model

$$\mathcal{H}_{XY} = -\sum_{\langle i,j \rangle} \cos(\theta_i - \theta_j), \tag{9}$$

where $\theta_i = \frac{2\pi q}{6}$, and $q = 0, 1, 2, 3, 4, 5$. The six-state clock model on a honeycomb lattice (dual triangular lattice) offers an approximate description of the triangular TFIM at weak field[3], i.e. towards the end of the anneal. We find the slope

$$m_{\mathrm{MC}} \propto t_a^{0.37}, \tag{10}$$

which is in close agreement with the observed slope on the QA. This leads us to hypothesize that a coarsening scenario past the quantum critical point dominates the KZM and governs the scaling behavior of the system.

To investigate this, we look at the scaling of the topological defects (Fig. 2b) on the triangular lattice (Fig. 4e) where we benchmark the lattice size 6 × 6 using MPS. The topological defects in this model correspond to polarized plaquettes where all the spins belonging to a plaquette point along the same

https://doi.org/10.1038/s41467-024-54701-4

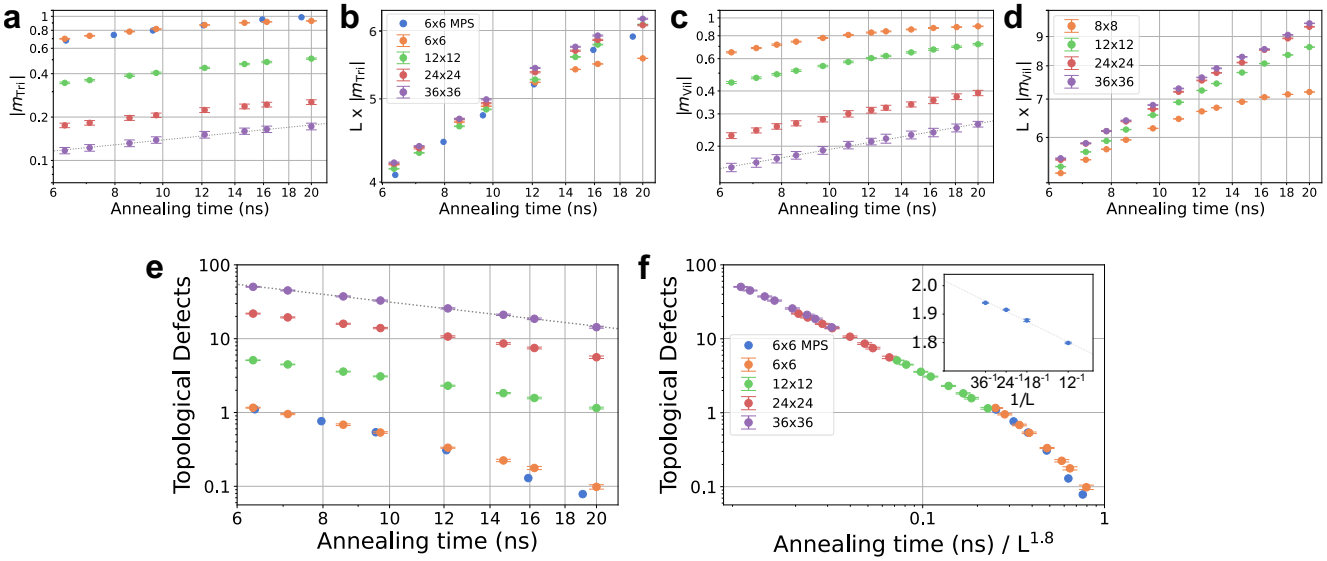

Fig. 4 | Scaling and collapse of order parameters and defect count. **a**, **b** Triangular OP scaling with annealing time, and its collapse upon scaling the y-axis by the system size L. **c**, **d** Same as **a**, **b** for the Villain OP. **e** Scaling of the number of topological defects (vortices and anti-vortices) in the triangular lattice with annealing time. **f** Horizontal collapse of the topological defects number, where the transition from linear to non-linear indicates a change in the underlying mechanism, as explained in the main text. Inset shows the fitting exponent for the data collapse. The fitting is plotted against $1/L$ where L is the smallest size included in the data collapse. It approaches a value close to 2 as $1/L \to 0$ which, as explained in the main text, indicates a volume-law scaling of the number of defects (grey line is a guide to the eye). Error bars represent $1 - R^2$ for the collapse fit. Source data are provided as a Source Data file.

direction. Our results indicate a scaling exponent

$$\rho \propto t_a^{-1.08(5)}, \tag{11}$$

again, in disagreement with the KZM prediction

$$\rho \propto t_a^{-\frac{d\nu}{1+z\nu}} = t_a^{-0.8}, \tag{12}$$

However, Eq. (11) is in close agreement with the coarsening expectation in an XY model[34] which predicts a scaling with an exponent equal to 1, up to logarithmic corrections. This supports our hypothesis that a coarsening mechanism dominates the system towards the end of the anneal.

Despite this, looking at Fig. 4f, we find a collapse of the topological defects at different sizes. The behavior of the collapse changes from a power-law for larger system sizes to exponential for the smallest system size 6 × 6. This indicates a change in the underlying mechanism governing the system dynamics, namely a crossover from KZM to a Landau-Zener regime as the correlation length approaches the system size. This crossover was also identified in QA results in one-dimensional chains[19]. The power-law fit, which can be seen to increase in the inset of Fig. 4f for larger systems sizes, suggests a volume-law scaling of defects. In 2D, volume-law corresponds to a scaling exponent equal to 2. We understand the correction to this scaling exponent as stemming from finite-size effects; for smaller systems, defects created near the boundaries come at a smaller energy cost.

Finally, we look at the magnetic correlations through the static structure factor (SF)

$$S(\mathbf{q}) = \frac{1}{N^2}\sum_{i=1}^{N}\sum_{j=1}^{N}\langle s_i s_j\rangle e^{-i\mathbf{q}\cdot(\mathbf{r}_i-\mathbf{r}_j)}, \tag{13}$$

for the triangular lattice, where s_i denotes the final spin output for site i. The SF offers a direct connection between the computational results and experiments on triangular TFIM magnets, such as the rare-earth (RE) heptatantalates ($RETa_7O_{19}$) using neutron diffraction and neutron Laue measurements[35]. Notably, the 2D XY-KT transition was observed in TFIM compound $TmMgGaO_4$, where the investigation of the melting of the magnetic order was performed as a function of thermal fluctuations (Fig. 5 in[36]).

Figure 5 a shows the SF evaluated for the 36 × 36 lattice at different annealing times up to 20 ns. We distinguish the six-peak hexagon typical of triangular order. We also observe how the peaks became sharper as the annealing time increased indicating higher order. We obtain the correlation lengths ξ as the inverse FWHM of the peaks and showcase how they scale with annealing time in Fig. 5b for the vertical (periodic, effective length $L/2$) and horizontal (open, length L) directions. We observe consistent behavior for the sizes L = 24 and 36 for both directions with the scaling exponent

$$\xi \propto t_a^{0.62(3)}, \tag{14}$$

as opposed to the KZM expectation

$$\xi \propto t_a^{\frac{\nu}{1+z\nu}} = t_a^{0.4}. \tag{15}$$

But again, our observed scaling is in agreement with the MC result (details in Methods)

$$\xi_{MC} \propto t^{0.55}, \tag{16}$$

further solidifying the coarsening argument.

Therefore, we conclude that a coarsening mechanism dominates KZM at later stages in the anneal and controls the post-critical dynamics of the systems, as seen through the scaling of the OPs (Eq. (7)), topological defects (Eq. (11)), and correlation lengths (Eq. (14)). While the quantum phase transition and its associated universality class govern the KZM scaling close to the critical regime, we find that the following coarsening dynamics are well-explained by the relaxation dynamics of the six-state clock model. Nonetheless, programmable QAs continue to prove their advantage as scalable coherent simulators for quantum systems.

Our experiment, when extended to finite temperature, can describe the BKT phase transition which is observed in many systems

https://doi.org/10.1038/s41467-024-54701-4

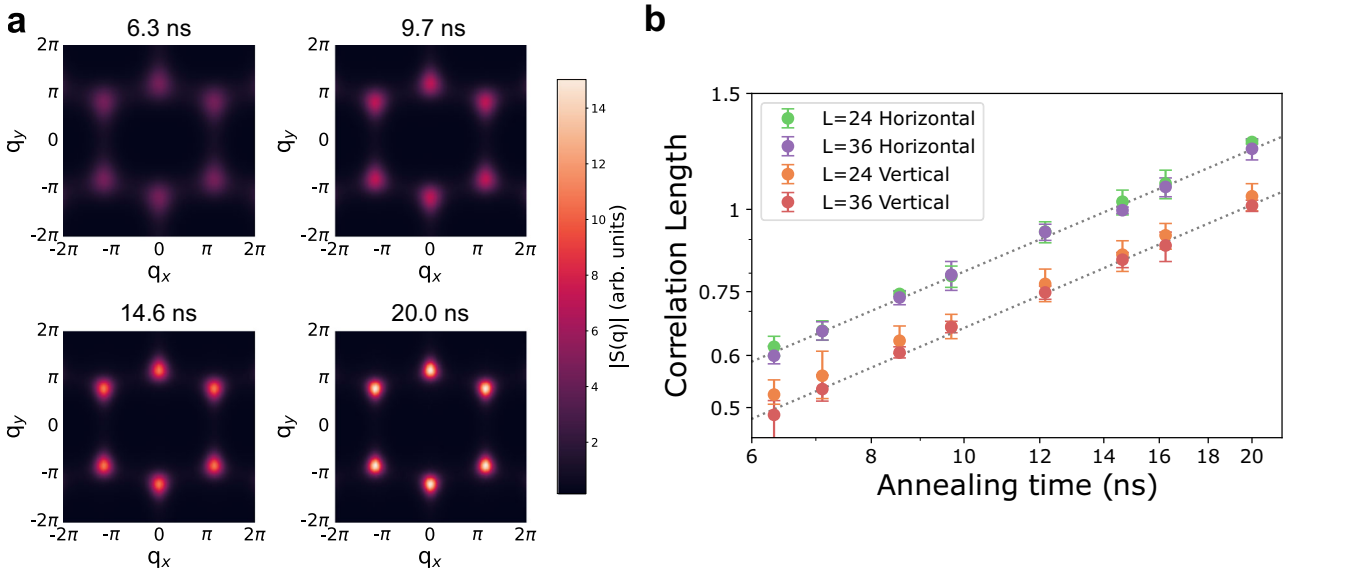

Fig. 5 | Static structure factor (SF) and correlation lengths. a The evolution of the SF $S(\mathrm{q})$ intensity for different annealing times evaluated on a 36 × 36 triangular lattice. $\mathrm{q}_{x(y)}$ is the momentum along the horizontal (vertical) direction which is open (periodic) with length L (L/2). **b** Horizontal and vertical Log-Log scaling of the correlation lengths evaluated on the two largest triangular lattice systems L = 24 and 36. Dashed lines correspond to best fits. Source data are provided as a Source Data file.

such as Helium films[37], Bose gases[38], and polariton systems[39]. Our experimental platform is also well-suited to study and simulate the 1D quantum axial-next-nearest-neighbors-Ising (ANNNI) model[40,41] (for a comprehensive discussion see[42]) which has received recent interest in its quench dynamics[43,44]. QAs can offer a new lens to investigate the existence and extent of the controversial ANNNI floating phase. In the future, our results could be tested on real experiments, for example with triangular Ising magnets such as $TmMgGaO_4$[36], subjected to the application of a transverse field close to the critical value Γ_c, with an AC field $\Gamma(\omega)$ where scaling laws would emerge as a function of ω (the quench time $\tau \propto 1/\omega$). After all, predicting the behavior of materials using quantum simulators, and benchmarking the quantum simulators against materials is the inevitable cycle for large-scale simulations, as classical methods will always have a hard time competing with the exponentially growing Hilbert space.

Methods

Quantum annealing

All quantum annealing data were taken from D-Wave Advantage 4.1 QA. The annealing schedule is depicted in Supplementary Fig. 2. We performed an iterative calibration refinement method, called shimming, to calibrate the qubits. The detailed shimming routines are explained in the next subsection. Each shimming iteration took 100 samples which may consist of multiple disjoint lattices depending on the lattice size (Supplementary Table 1). We performed 1500 shimming iterations for each lattice size at every anneal time and collected several samples at the end after the shimming parameters stabilized. The specific numbers of disjoint lattices per sample and samples collected for computations are shown in Supplementary Table 1.

Shimming

Frustrated systems are extremely sensitive to noise perturbations stemming from the fact that these perturbations break their vast degeneracy. For this reason, following[19,45] we perform three hardware calibration measures:

- Flux Bias Shim
- Couplers' Strength Shim
- Anneal Offset Shim

which we now explain. For shimming plots refer to Supplementary Figs. 3 and 4. For lattice sizes with multiple copies of disjoint lattices, shimming is performed based on their combined statistics.

Flux bias shim. The Hamiltonian, Eq. (2), has zero longitudinal magnetic field. Therefore, the expected magnetization of each qubit should be zero after measuring a statistical number of samples. We iteratively adjust the flux bias for each qubit where at the k-th iteration, with the average magnetization for qubit i of the previous iteration being $\langle m\rangle_i^k$, we set the flux bias to

$$\phi_i^k = \phi_i^{k-1} - \delta_\phi \langle m\rangle_i^k, \tag{17}$$

$\delta_\phi = 2e - 6$. This flux bias corrects the behavior of the qubits and gets rid of any internal bias to point in a specific direction.

Couplers' strength shim. Given a coupler J_{ij}, its probability to be frustrated is

$$f_{ij} = (\mathrm{sign}(J_{ij})\langle m_i m_j\rangle + 1)/2. \tag{18}$$

The symmetries present in the problem will give some expectations of what the average frustration should be for the different couplers. For example, a 1D FM ring is rotationally invariant, thus all the couplers should have the same frustration probability and are said to be in the same orbit. For our problem, the couplers are arranged in a cylinder with alternating FM and AFM bonds along the periodic direction (Fig. 1c). Therefore, every other coupler in the same column belongs to the same orbit.

The orbit that contains f_{ij} has the average frustration probability:

$$f_{O_{ij}} = \sum_{i'j' \in O_{ij}} \frac{f_{i'j'}}{|O_{ij}|}, \tag{19}$$

where O_{ij} is the orbit containing the coupler f_{ij}, and $|O_{ij}|$ is its size. At the k-th iteration, we adjust the coupler strength as

$$J_{ij}^k = J_{ij}^{k-1} + \mathrm{sign}(J_{ij})\delta_f(f_{ij} - f_{O_{ij}}), \tag{20}$$

$\delta_f = 2.5e - 3$. This procedure ensures that all symmetrically equivalent couplers are acting with the same effective strength.

Anneal offset shim. The qubits and couplers of Advantage 4.1 QA are arranged on 8 different annealing lines that perform the annealing independently from $s = 0$ to $s = 1$. For the extremely fast anneals we are performing, the 8 annealing lines may not be in sync with discrepancies ranging from a fraction of a nanosecond to one nanosecond. To correct for this, we obtain the annealing offsets from a 1D FM ring where we enforce the average frustration per annealing line to be equal, as was done in ref. 19.

MPS simulation

In this work, MPS simulations were performed using the ITensor Julia library[46,47]. The triangular lattice was simulated using open-ended cylinders, with the axis along the x direction and one of the three bond directions aligned along the y axis, realizing a YC-6 cylinder[48] (see Fig. 1a). Time evolution was performed using the time-dependent variational principle (TDVP) algorithm[49] with a two-site update where a convergence for the computed physical quantities was observed at a bond dimension $\chi = 150$. Care was taken (by playing with the size of the time step dt) to ensure that the bond dimension grows with time since the algorithm starts from the product state $\prod_i |\rightarrow\rangle_i$. We also compared different methods to simulate the anneal dynamics. Supplementary Fig. 5 shows comparison analysis as a function of the time step size dt for the TDVP method against the W_I and W_{II} approximations introduced in ref. 50. Clearly, the ability to use large time steps makes TDVP the best choice in terms of speed and accuracy. The initial state is the Bell state (Eq. (3)), and the Hamiltonian parameters $\Gamma(s)$ and $\mathcal{J}(s)$ followed the exact annealing schedule of Advantage 4.1. The relationship between the simulation time t_{sim} and the annealing time in ns t_a is $t_{sim} = \pi t_a$, and a time step of $dt = 0.05$ was used. The relevant physical quantities studied in the main text (OPs and structure factors) are then computed by sampling the wave-function at the end of the annealing process which collapses it into the computational basis[51]. We do not simply obtain expectation values which could be deceptive for symmetry unbroken superposition states obtained in simulations as opposed to symmetry broken states defining our OPs. For example, a quantum ferromagnetic ground state $|\uparrow\uparrow\uparrow\ ..\rangle + |\downarrow\downarrow\downarrow\ ..\rangle$ has $m = \sum_i \langle\sigma_i^z\rangle = 0$, but measuring and collapsing the state correctly yields $|m| = 1$.

Statistical methods

Error bars from Fig. 4 are generated through a bootstrap method where we first average the observables from each QPU call of 100 samples, and then compute the standard deviation out of these averages. To compute confidence intervals for correlation lengths in Fig. 5, we used *lmfit*'s[52] *conf_interval* method. It employs F-test in Eq. (21) to compare χ^2 statistics of the null model with our best-found fitting parameters to an alternate model where one of the parameters is fixed.

$$F(P_{fix}, N-P) = \left(\frac{\chi_f^2}{\chi_0^2} - 1\right)\frac{N-P}{P_{fix}} \tag{21}$$

Here N is the number of data points and P is the number of parameters of the null model. P_{fix} is the number of fixed parameters.

To obtain the best-fit slopes, we bootstrap by resampling the data points of the largest system size (36×36) 200 times. We then report the mean and the 95% confidence interval of the bootstrap.

Monte Carlo coarsening simulation

Here we compare dynamic scaling of the order parameter and correlation length with a quasi-classical coarsening scenario, as hypothesized to dominate scaling due to postcritical dynamics. In the perturbative regime ($\Gamma \ll \mathcal{J}$), the effective model is a two-dimensional six-state "clock" XY model[12,14]. The XY spins lie on the plaquettes of the triangular lattice, i.e., on the sites of the dual honeycomb lattice.

To simulate a coarsening dynamics we proceed with an absorbing Markov-chain Monte Carlo (MCMC) process with both two-site and one-site updates, to avoid local minima. The energy of the state $\boldsymbol{\theta} = \{\theta_1, ..., \theta_N\}$ is calculated as

$$\mathcal{H}_{XY} = -\sum_{\langle i,j\rangle} \cos(\theta_i - \theta_j). \tag{22}$$

At each time step, we first process all edges of the model in random order, proposing new angles uniformly at random for both endpoints, and accepting if and only if the energy is not increased. We then process all individual spins in random order, proposing new angles one at a time.

This was performed on a honeycomb lattice with $L = 120$ and fully periodic boundary conditions, constructed from a square lattice by deletion of edges. 100 independent replicas were run for 1000 time steps. We computed $\langle m\rangle$ as the average rotor value (unit vectors with angle θ_i) and computed the correlation between two spins as $\cos(\theta_i - \theta_j)$ (Supplementary Fig. 6). Correlation lengths were computed based on distances 5 to 20.

Correlation length extraction

Correlation lengths were extracted from the peaks of the structure factor (Eq. (13)) by fitting to the Pseudo–Voigt function

$$V(x) = \eta G(x) + (1-\eta)L(x), 0 \le \eta \le 1, \tag{23}$$

where $G(x)$ is the Gaussian function $\frac{1}{\sqrt{2\pi}\sigma} e^{-\frac{(x-x_0)^2}{2\sigma^2}}, \sigma = \frac{\Gamma}{2\sqrt{2\ln 2}}$ and $L(x)$ is the Lorenzian function $\frac{1}{\pi}\cdot\frac{\Gamma/2}{(x-x_0)^2+(\Gamma/2)^2}$. Here x_0 is the maximum momentum position and Γ is the full-width at half maximum (FWHM) from which the correlation length follows as $\xi = 1/\Gamma$.

Data availability

The data generated in this study have been deposited in the GitHub repository[53] https://github.com/jxsoortha/Quantum-Quench-Dynamics-of-Geometrically-Frustrated-Ising-Models. Source data are provided with this paper.

References

1. Schmidt, B. & Thalmeier, P. Frustrated two dimensional quantum magnets. *Phys. Rep.* **703**, 1–59 (2017). Frustrated two dimensional quantum magnets.
2. Shaginyan, V. R. et al. Theoretical and experimental developments in quantum spin liquid in geometrically frustrated magnets: A review. *J. Mater. Sci.* https://link.springer.com/article/10.1007/s10853-019-04128-w (2019).
3. Moessner, R. & Sondhi, S. L. Ising models of quantum frustration. *Phys. Rev. B* **63**, 1–19 (2001).
4. Anderson, P. W. Resonating valence bonds: A new kind of insulator? *Mater. Res. Bull.* **8**, 153–160 (1973).
5. Savary, L. & Balents, L. Quantum spin liquids: a review. *Rep. Prog. Phys.* **80**, 016502 (2016).
6. Teo, J. C. & Hughes, T. L. Topological defects in symmetry-protected topological phases. *Annu. Rev. Condens. Matter Phys.* **8**, 211–237 (2017).
7. Blankschtein, D., Ma, M., Berker, A. N., Grest, G. S. & Soukoulis, C. M. Orderings of a stacked frustrated triangular system in three dimensions. *Phys. Rev. B* **29**, 5250–5252 (1984).
8. Blankschtein, D., Ma, M. & Berker, A. N. Fully and partially frustrated simple-cubic Ising models: Landau-Ginzburg-Wilson theory. *Phys. Rev. B* **30**, 1362–1365 (1984).

9. Sachdev, S. Quantum phase transitions. *Phys. world* **12**, 33 (1999).
10. Jalabert, R. A. & Sachdev, S. Spontaneous alignment of frustrated bonds in an anisotropic, three-dimensional Ising model. *Phys. Rev. B* **44**, 686–690 (1991).
11. Moessner, R., Sondhi, S. L. & Chandra, P. Two-dimensional periodic frustrated ising models in a transverse field. *Phys. Rev. Lett.* **84**, 4457–4460 (2000).
12. Isakov, S. V. & Moessner, R. Interplay of quantum and thermal fluctuations in a frustrated magnet. *Phys. Rev. B* **68**, 104409 (2003).
13. Villain, J. Spin glass with non-random interactions. *J. Phys. C: Solid State Phys.* **10**, 1717 (1977).
14. King, A. D. et al. Observation of topological phenomena in a programmable lattice of 1,800 qubits. *Nature* **560**, 456–460 (2018).
15. Kosterlitz, J. & Thouless, D. Ordering, metastability and phase transitions in two-dimensional systems 1973. *J. Phys.: Condens. Matter* **6**, 1181 (1973).
16. King, A. D. et al. Scaling advantage over path-integral Monte Carlo in quantum simulation of geometrically frustrated magnets. *Nat. Commun.* **12**, 1113 (2021).
17. Bauza, H. M. & Lidar, D. A. Scaling advantage in approximate optimization with quantum annealing. https://doi.org/10.48550/arXiv.2401.07184 (2024).
18. Narasimhan, P. et al. Simulating the transverse field Ising model on the kagome lattice using a programmable quantum annealer. *Phys. Rev. B* **110**, 054432 (2024).
19. King, A. D. et al. Coherent quantum annealing in a programmable 2000 qubit Ising chain. *Nat. Phys.* **18**, 1324–1328 (2022).
20. Kibble, T. W. Topology of cosmic domains and strings. *J. Phys. A: Math. Gen.* **9**, 1387 (1976).
21. Zurek, W. H. Cosmological experiments in superfluid helium? *Nature* **317**, 505–508 (1985).
22. Keesling, A. et al. Quantum kibble-zurek mechanism and critical dynamics on a programmable rydberg simulator. *Nature* https://doi.org/10.1038/s41586-019-1070-1 (2019).
23. Ebadi, S. et al. Quantum phases of matter on a 256-atom programmable quantum simulator. *Nature* https://doi.org/10.1038/s41586-021-03582-4 (2021).
24. King, A. D. et al. Quantum critical dynamics in a 5000-qubit programmable spin glass. *Nature* http://arxiv.org/abs/2207.13800 (2022).
25. King, A. D. et al. Computational supremacy in quantum simulation. https://doi.org/10.48550/arXiv.2403.00910 (2024).
26. Manovitz, T. et al. Quantum coarsening and collective dynamics on a programmable quantum simulator. https://arxiv.org/abs/2407.03249 (2024).
27. Andersen, T. I. et al. Thermalization and criticality on an analog-digital quantum simulator. https://arxiv.org/abs/2405.17385 (2024).
28. Schumm, G. et al. Primary and secondary order parameters in the fully frustrated transverse-field Ising model on the square lattice. *Phys. Rev. B* **109**, L140408 (2024).
29. Liang, S. & Pang, H. Approximate diagonalization using the density matrix renormalization-group method: A two-dimensional-systems perspective. *Phys. Rev. B* **49**, 9214–9217 (1994).
30. Stoudenmire, E. M. & White, S. R. Studying two-dimensional systems with the density matrix renormalization group. *Annu. Rev. Condens. Matter Phys.* **3**, 111–128 (2012).
31. Campostrini, M., Hasenbusch, M., Pelissetto, A., Rossi, P. & Vicari, E. Critical behavior of the three-dimensional XY universality class. *Phys. Rev. B* **63**, 214503 (2001).
32. Chester, S. M. et al. Carving out OPE space and precise O(2) model critical exponents. *J. High. Energy Phys.* **2020**, 142 (2020).
33. Sondhi, S. L., Girvin, S. M., Carini, J. P. & Shahar, D. Continuous quantum phase transitions. *Rev. Mod. Phys.* **69**, 315–333 (1997).
34. Yurke, B., Pargellis, A. N., Kovacs, T. & Huse, D. A. Coarsening dynamics of the xy model. *Phys. Rev. E* **47**, 1525–1530 (1993).
35. Arh, T. et al. The Ising triangular-lattice antiferromagnet neodymium heptatantalate as a quantum spin liquid candidate**.** *Nat. Mater.* **21**, 416–422 (2022).
36. Li, H. et al. Kosterlitz-Thouless melting of magnetic order in the triangular quantum Ising material TmMgGaO4. *Nat. Commun.* **11**, 1111 (2020).
37. Bishop, D. J. & Reppy, J. D. Study of the superfluid transition in two-dimensional ^{4}He films. *Phys. Rev. Lett.* **40**, 1727–1730 (1978).
38. Hadzibabic, Z., Krüger, P., Cheneau, M., Battelier, B. & Dalibard, J. Berezinskii-kosterlitz-thouless crossover in a trapped atomic gas. *Nature* **441**, 1118–1121 (2006).
39. Dagvadorj, G., Comaron, P. & Szymańska, M. H. Unconventional berezinskii-kosterlitz-thouless transition in the multicomponent polariton system. *Phys. Rev. Lett.* **130**, 136001 (2023).
40. Rieger, H. & Uimin, G. The one-dimensional ANNNI model in a transverse field: analytic and numerical study of effective Hamiltonians. *Z. f.ür. Phys. B Condens. Matter* **101**, 597–611 (1996).
41. Allen, D., Azaria, P. & Lecheminant, P. A two-leg quantum ising ladder: a bosonization study of the annni model. *J. Phys. A: Math. Gen.* **34**, L305 (2001).
42. Dutta, A. et al. *Quantum Phase Transitions in Transverse Field Spin Models: From Statistical Physics to Quantum Information* (Cambridge University Press, 2015).
43. Haldar, A. et al. Signatures of quantum phase transitions after quenches in quantum chaotic one-dimensional systems. *Phys. Rev. X* **11**, 031062 (2021).
44. Robertson, J. H., Senese, R. & Essler, F. H. L. A simple theory for quantum quenches in the ANNNI model. *SciPost Phys.* **15**, 032 (2023).
45. Chern, K., Boothby, K., Raymond, J., Farré, P. & King, A. D. Tutorial: calibration refinement in quantum annealing. *Front. Comput. Sci.* **5**, 1238988 (2023).
46. Fishman, M., White, S. R. & Stoudenmire, E. M. The ITensor software library for tensor network calculations. *SciPost Phys. Codebases*. https://scipost.org/10.21468/SciPostPhysCodeb.4 (2022).
47. Fishman, M., White, S. R. & Stoudenmire, E. M. Codebase release 0.3 for ITensor. *SciPost Phys. Codebases* 4–r0.3 https://scipost.org/10.21468/SciPostPhysCodeb.4-r0.3 (2022).
48. Zhu, Z. & White, S. R. Spin liquid phase of the $s = \frac{1}{2} J_1 - J_2$ heisenberg model on the triangular lattice. *Phys. Rev. B* **92**, 041105 (2015).
49. Haegeman, J., Lubich, C., Oseledets, I., Vandereycken, B. & Verstraete, F. Unifying time evolution and optimization with matrix product states. *Phys. Rev. B* **94**, 165116 (2016).
50. Zaletel, M. P., Mong, R. S. K., Karrasch, C., Moore, J. E. & Pollmann, F. Time-evolving a matrix product state with long-ranged interactions. *Phys. Rev. B* **91**, 165112 (2015).
51. Stoudenmire, E. M. & White, S. R. Minimally entangled typical thermal state algorithms. *N. J. Phys.* **12**, 055026 (2010).
52. Newville, M., Stensitzki, T., Allen, D. B. & Ingargiola, A. LMFIT: Non-Linear Least-Square Minimization and Curve-Fitting for Python. Zenodo (2014).
53. Xu, H. Quantum-quench-dynamics-of-geometrically-frustrated-ising-models. https://github.com/jxsoortha/Quantum-Quench-Dynamics-of-Geometrically-Frustrated-Ising-Models (2024).

Acknowledgements

The authors would like to thank Anders Sandvik for insightful discussions. A.A. and A.B. acknowledge funding from Quantum Science Center (QSC), a National Quantum Science Initiative of the Department Of Energy (DOE), managed by Oak Ridge National Laboratory (ORNL) managed under contract DE-AC05-00OR22725 for the theory effort in the paper and access to Purdue Bell clusters. H.X. and the work with D-Wave, are supported by the Center for Quantum Technologies (CQT) under the Industry-University Cooperative Research Center (IUCRC) Program at the US National Science Foundation (NSF) under Grant

No. 2224960. The team, especially H.X., thanks Alex Pothen for help with the IUCRC funding and guidance. A.B. thanks D-Wave for access to fast annealing protocols in their devices. A.N. was supported by Natural Sciences and Engineering Research Council of Canada (NSERC) Alliance Quantum Program (Grant ALLRP-578555), CIFAR and the Canada First Research Excellence Fund, Quantum Materials and Future Technologies Program. We gratefully acknowledge supporting contributions from technical and non-technical staff at D-Wave.

Author contributions

A.D.K. and A.B. conceived and supervised the project. A.A., H.X., and A.D.K. produced the findings of the work. A.N., A.A., and W.B. performed MPS experiments and analysis. H.X. and A.D.K. performed quantum simulations. A.A. and H.X. produced the first draft with supervision from A.B. and A.D.K. All authors discussed the results and contributed to the final manuscript.

Competing interests

W.B. and A.D.K. are employees and stockholders of D-Wave Quantum Inc. and declare a competing interest on that basis. The remaining authors declare no competing interests.

Additional information

Supplementary information The online version contains supplementary material available at https://doi.org/10.1038/s41467-024-54701-4.

Correspondence and requests for materials should be addressed to Andrew D. King or Arnab Banerjee.

Peer review information *Nature Communications* thanks Bikas Chakrabarti, Hunpyo Lee and the other, anonymous, reviewer for their contribution to the peer review of this work. A peer review file is available.